

Prediction of an alternative route to polymeric carbon dioxide: A metastable energetic material

Reetam Paul¹, Jonathan C. Crowhurst¹, and Stanimir A. Bonev^{1,*}

¹Lawrence Livermore National Laboratory, 7000 East Avenue, Livermore, CA 94550

*bonev2@llnl.gov

ABSTRACT

The use of pressure to obtain new materials that can be recovered under ambient conditions is a central problem in high-pressure physics. Despite decades of research, this goal has only been achieved in the laboratory for a few notable examples, such as diamond and cubic boron nitride. An area of significant interest is the transformation under compression of light-element molecular compounds to extended covalent-bonded (polymeric) solids. Among them, CO₂ has been extensively studied because of its status as a prototypical simple molecular system with a rich phase diagram and due to its fundamental role in Earth's physics and chemistry. One of its polymeric crystalline phases, accessible at extreme pressures and temperatures, has been recently quenched to ambient pressure, but below room temperature. Here we report *ab initio* calculations predicting that isothermal compression of a carbon monoxide and oxygen mixture (CO+O₂), rather than the compound CO₂, lowers the onset of C-polymerization at room temperature from ~ 118 GPa to ~ 7 GPa (complete by ~ 23 GPa). Moreover, it leads to the formation of an intrinsically different polymer with enhanced metastability. We predict that this dense phase is an energetic material which can potentially be recovered to ambient pressure and temperature.

In the high-pressure sciences, there have been discoveries of exotic crystalline phases of even simple elements such as Ca¹, Na², and Li³. However, almost without fail, thermodynamic or kinetic effects lead to the breakdown of such exotic phases upon decompression (relaxation) and their practical applications as superhard⁴ or high-energy-density (HED) materials have been precluded, albeit with a few exceptions such as diamond⁵ and cubic boron nitride^{6,7}.

The confluence of high-pressure physics and energetic materials research has led to the prediction that the high-pressure (~ 110 GPa) and high-temperature (~ 2000 K) synthesis of cubic gauche nitrogen (*cg*-N, space group $I2_13$)^{8,9} would lead to an energetic material having upper end estimates of energy content more than twice that of TNT (>10 kJ/g), undoubtedly the most energetic non-nuclear composition in existence. Practical use would, of course, depend on developing a method for synthesizing the material at ambient pressure and temperature, which has very recently been suggested¹⁰, as all attempts at decompression-based recovery have failed. The materials further explored in this category include compressed phases of N-rich compounds^{8,11–15}, CO₂^{16–22,22–28}, CH₄²⁹, NH₃^{30,31}, and CO^{32–34}. They form extended covalent-bonded (polymeric) solids that, if recovered to ambient conditions, would be in a high-energy metastable state. A subsequent transition to a thermodynamically stable phase would release a large amount of energy. Naturally, much research has focused on attempts to make the synthesis conditions more accessible while increasing the HED content and ambient-condition metastability of the high-pressure phases. These requirements are often conflicting.

Carbon dioxide was one of the first molecular systems that was shown to polymerize under compression^{35,36}. Given its fundamental nature and importance for understanding the physics and chemistry of the Earth, its phase diagram has been of particular interest to the high-pressure research community^{17,37–39}. Below 200 K and at ambient pressure, CO₂ exists in phase I as a molecular solid ‘dry ice’ cubic structure (*Pa3*). At pressures above ~ 12 GPa, CO₂-I transforms to the molecular CO₂-III (*Cmca*), CO₂-II (*P4₂/mnm*) or CO₂-IV (*Pbcn*), in increasing order of temperature^{16,17}. Thereafter, the picture becomes somewhat uncertain. A fully covalent-bonded CO₂-V structure was obtained above 40–60 GPa with heating up to 1800 K, and reported as either tridymite (high temperature polymorph of silica/SiO₂, tetrahedrally bonded/fourfold-coordinated)-type (*P2₁2₁2₁*) at higher temperatures⁴⁰ or an extended-solid cristobalite-type (*I4-2d*) at lower temperatures^{25,41}. Metadynamics simulations²² starting from CO₂-III at ~ 80 GPa and <300 K suggest an intermediate *Pbca* ultimately evolving to an α -cristobalite-like (*P4₁2₁2*) fourfold-coordinated structure, whereas CO₂-II at ~ 60 GPa and ~ 600 K transforms to a fully tetrahedral, layered structure (*P4m2*). However, experimental observations²¹ reported a fully covalent extended-solid sixfold-coordinated stishovite-type CO₂-VI (*P4₂/mnm*) obtained directly by compressing CO₂-II above 50 GPa and at 530–650 K. There have also been predictions by simulations^{19,42} and observations in laser-heated conditions⁴³ above 40 GPa of an amorphous phase called carbonia/*a*-CO₂. A combination of experiments and simulations⁴⁴ have shown that the actual nature of CO₂ in the 40–100 GPa region is a mixture of three- and four-fold coordinated metastable phases, manifesting as *a*-CO₂, rather than

any particular well-defined fully tetrahedral phase. Recent attempts to recover polymeric crystalline CO₂-V (*P*₂₁2₁2₁)⁴⁵ have shown that the recovered product decays to dry ice/CO₂-I (*Pa*3) at 185 K. As such, recovering polymeric CO₂ to atmospheric pressure at room temperature has been hitherto elusive²⁷.

In general, pressure-induced polymerization of molecular compounds can be divided into two types, thermodynamic and kinetic transitions. The former takes place between phases that are in thermodynamic equilibrium. The compression of CO₂ and N₂ until polymerization falls into this category. Here, the amount of energy stored in the polymeric phases creates a trade-off with the accessibility of synthesis conditions. In the second type, the transition is from or to a phase which is metastable (i.e. a high-energy state). Thus, the kinetic barrier that separates the molecular and polymeric phases can be overcome at relatively low pressure. This is the case for CO, where the polymeric (*p*-CO) rather than the molecular phase is the stable one under ambient conditions, and the onset of the transition is only at around 5 GPa at 300 K. However, the usefulness of *p*-CO as a HED material is limited by the fact that its relevant exothermic reaction, namely the decomposition of *p*-CO to CO₂^(g) + C, contains a product (C) with a relatively high formation energy³³.

The challenge and a key for discovering a useful material is to combine the benefits of the two types of transitions. Systems such as polymeric CO₂ (*p*-CO₂) and *cg*-N are compelling due to the significant energy differential between these and their stable molecular phases at ambient pressure. However, to reduce the transition pressures, we wish to arrive at one of these polymeric phases via a kinetic transition from a high-energy state compared to their molecular phases. These considerations have motivated us to investigate the polymerization of a mixture of CO and O₂, stoichiometrically equivalent to the compound CO₂.

Another reason for evaluating this system is the expectation that amorphous systems offer more possibilities to achieve high metastability. First, decompression of high-pressure covalent crystalline phases can cause significant bond strains, leading them to become dynamically unstable. Second, kinetic barriers depend on the atomic arrangements, and amorphous solids have higher degrees of freedom for such arrangements.

Here we show that isothermal compression of a mixture of CO and O₂ at 300 K leads to a polymer stoichiometrically equivalent to *p*-CO₂, but accessible at much lower pressure than when compressing molecular CO₂ (*m*-CO₂). Importantly, the resulting amorphous polymer is structurally different from the known *p*-CO₂ phases and exhibits higher degree of metastability. Our study indicates that it can be stabilized at even elevated temperatures at near-atmospheric pressure. In the next section we describe the first-principles simulations leading to this prediction, followed by an analysis of structural and thermodynamics properties and metastability, comparative with that of the relevant solid CO₂ phases.

Results

Prediction of polymerization and recovery at 300 K

A gaseous mixture of molecular CO and O₂ was initially equilibrated using *ab initio* molecular dynamics (AIMD) simulations at ambient temperature and pressure conditions. It was then isothermally compressed along the 300 K isotherm. This approach results in the simulation of amorphous, rather than crystalline, polymeric high-pressure phases. It is intended to mimic experimental conditions, and in the case of CO was shown to agree well with measurements³³.

As detailed in the following sections, simulations were performed using (1) different numbers of atoms (as high as 864) to ensure size convergence and (2) various exchange-correlation functionals to confirm that the results are not artifacts of the functional choice. Unless specified otherwise, the discussion refers to the calculations with 432-atom supercells using the PBE exchange-correlation functional with DFT-D3 (zero damping)⁴⁶ semi-local dispersion forces. A full description of computational details can be found in the Methods section and Tables S1-S2 in Supplementary Discussion 1.

In these simulations, the onset of pressure-induced polymerization is predicted at approximately 7 GPa (~80% of ambient cell volume). The transformation is gradual; the early polymeric phase consists of broken chains and transient 4-member C–O rings. By ~23 GPa, complete polymerization of the CO molecules is observed (denoted as the *p_a* phase), characterized by –O(CO)– chains linking either planar or non-planar 5-member (C,O) rings and 6-member (C,O) rings. A visualization of the amorphous *p_a* phase with fully-polymerized C atoms is shown in Fig. 1a. The fraction of carbon and oxygen atoms locked in different bonding configurations in chains and rings is shown in Fig. 1b as a function of the simulation cell size (see Supplementary Discussion 2 for further details). The 432-atom simulations are well-converged with respect to equilibrated pressure and bonding statistics. Finally, upon decompression (simulated for a total of 10.1 ps) from the highest compressed configuration at ~32 GPa along the 300 K isotherm, the *p_a* phase is retained all the way to ambient pressure with only a minor change in the bonding statistics (see Supplementary Figs. S1-S3).

To explore the possibility of formation, under isothermal compression, of [CO+O₂]-like crystalline structures that are energetically competitive with the *p_a* phase, we complemented the above approach with constrained metadynamics simulations. In this methodology, the CO and O₂ bond lengths were constrained to remain close to their unreacted equilibrium values. The simulations yielded two polymeric crystalline phases: one with an 84-atom unit cell (space group *Pbcn*) and another one

with a 36-atom unit cell ($P1$), denoted as p_{c1} and p_{c2} , respectively. A visualization of these phases and a comparison of their enthalpies to that of the amorphous p_a are shown in Fig. 1c. They are energetically favorable to p_a only in a small pressure region below 10 GPa, and when subjected to constant-pressure AIMD, they become disordered (see Supplementary Fig. 4 for visualization). Upon further compression, they amorphize to structures identical to p_a . Therefore, we conclude that while intermediate crystalline phases are possible, isothermal compression at 300 K of a mixture of molecular CO and O₂ leads to the amorphous phase p_a at pressure above 10 GPa, which will be the principal focus of this paper. Note that all these phases are metastable relative to known molecular and polymeric CO₂ phases, as will be discussed in the following sections.

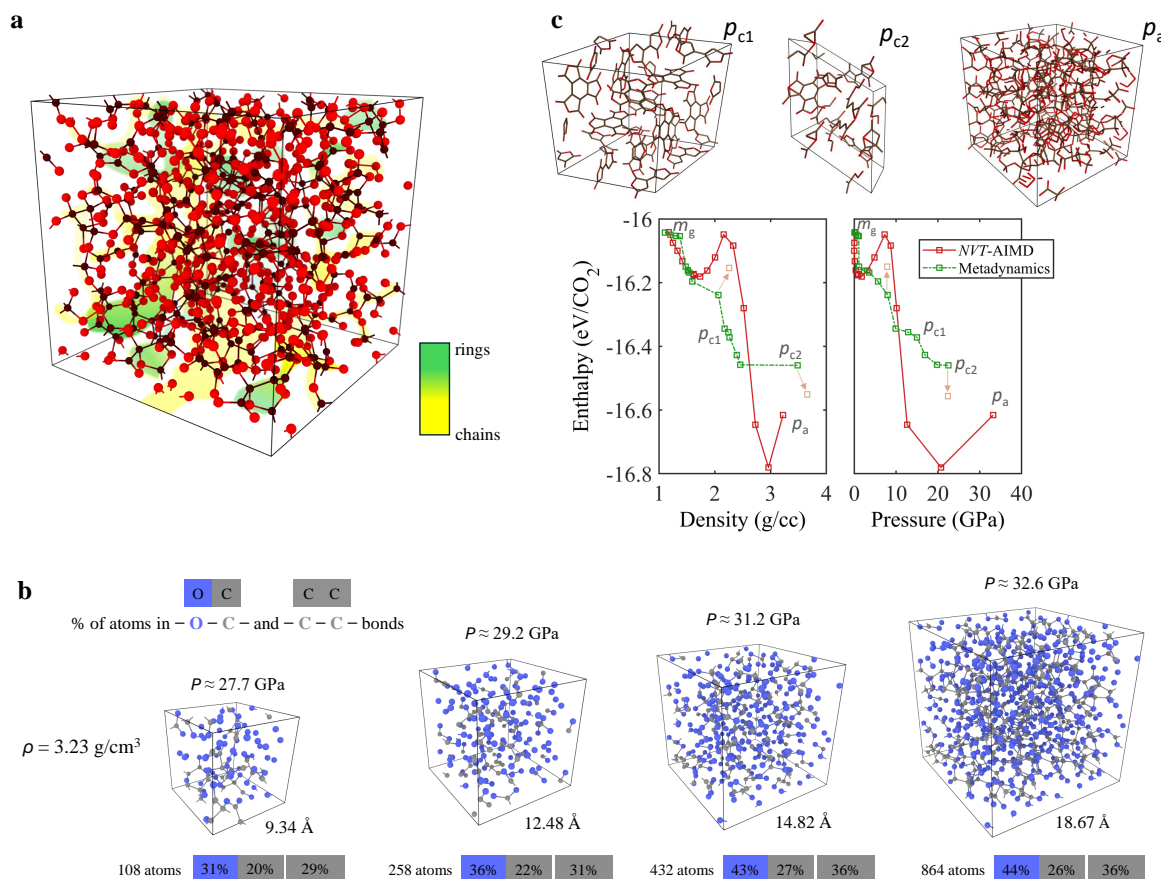


Fig. 1 Results from isothermal compression of CO+O₂ mixtures using NVT-AIMD simulations along the $T = 300$ K isotherm. **a** Polymerized amorphous product in an 864-atom cell at 32.6 ± 0.7 GPa and $\rho = 3.23$ g/cc after simulation time of 11 ps at 300 K. Red and brown spheres indicate oxygen and carbon atoms, respectively, with chain and ring regions color-coded as shown. **b** Comparison of simulation results obtained with different cell sizes at $\rho = 3.23$ g/cc. Shown are the percentage of atoms locked in $-O-C-$ and $-C-C-$ bonds, and the equilibrated pressure P . Convergence is reached with 432-atom simulations. Violet and gray spheres correspond to oxygen and carbon atoms, respectively. The dimensions of the cubic box simulation cells are shown in Angstroms. **c** Starting from a molecular gaseous mixture of CO and O₂, labeled as phase m_g , the resulting phases from AIMD and metadynamics searches are shown in perspective view. The polymeric crystalline phases p_{c1} (84-atom $Pbcn$) and p_{c2} (36-atom $P1$) were obtained from constrained metadynamics searches. At pressures above 10 GPa, the polymeric amorphous phase p_a is energetically preferred, as can be seen in the enthalpy versus pressure and density plots. The brown arrows and markers point to the change in the enthalpy and density when NPT-AIMD simulations are performed on the crystalline phases.

A consideration when analyzing the stoichiometry of the compressed p_a polymer is to determine if there are any residual unreacted molecules remaining in the system. We observe that at around 30 GPa, when the C atoms are fully polymerized,

there are a few remaining O_2 molecules. Upon further compression, these residual molecules form oxygen chains, and at ~ 88 GPa, they attach to the remaining polymer without affecting its structure. We have investigated several different recipes for the formation of polymers with exact CO_2 stoichiometry, including over- and undersaturation with O_2 , compression along a higher temperature isotherm, and heating the p_a phase at 32 GPa followed by further compression. The results for the enthalpy, stoichiometry, and structural details of the phases obtained in these computational experiments are summarized in Fig. 2.

As evident from the data, compressing the gas mixture at higher temperature lowers the polymerization pressure and brings the polymer closer to CO_2 stoichiometry near 30 GPa. Oxygen undersaturation delays the onset of polymerization, while oversaturation does not accelerate it. On the other hand, oversaturation reduces the pressure at which oxygen is fully locked up in the polymeric structure. Thus, as a recipe for experimentalists to achieve a polymer with exact CO_2 stoichiometry, we propose a combination of oversaturation and compression at elevated temperatures starting from below 7 GPa. However, in the remainder of this paper, the analysis will focus on the properties derived from the p_a phase at 32 GPa, corresponding to $CO_{1.88}+O_2^{(s)}$. Having a few non-reacted O_2 molecules, it provides a lower bound for the stability of the recovered polymer and its energy content.

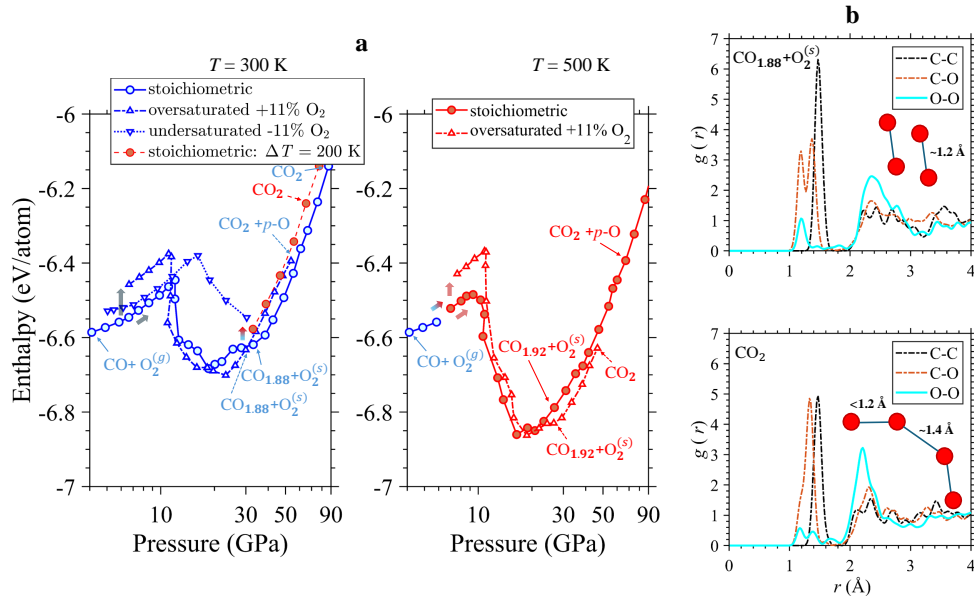


Fig. 2 a Enthalpy versus pressure plots for 192-atom NVT-AIMD simulations along compression trajectories at (left) 300 K and (right) 500 K. Plotted are results for systems with stoichiometric CO_2 mixtures, as well as such with 11% over- and under-saturation of oxygen. The red symbols in the left panel indicate a system heated to 500 K at about 32 GPa and then further compressed. The remaining results are for isothermal compressions starting from below 7 GPa. The labels to selected points indicate the stoichiometry of the polymeric phase achieved at various pressures and the presence of unreacted ($O_2^{(s)}$) or polymerized ($p-O$) oxygen. **b** Radial distribution function, $g(r)$, for $CO_{1.88}+O_2^{(s)}$ (top) and CO_2 (bottom) along the 300 K compression trajectory at approximately 32 and 88 GPa, respectively. The inset cartoons show how the remaining unreacted O_2 molecules at 32 GPa link up to form chains in fully-polymerized $CO+O_2$ at 88 GPa.

Finally, we verify the mechanical stability of the recovered polymeric phase, which we denote as $p_{a,rc}$. The computed phonons do not exhibit any imaginary modes (see Supplementary Fig. S5), which indicates that $p_{a,rc}$ is metastable. However, it is important to note that this standard approach does not provide information about the magnitude of kinetic barriers and, consequently, the temperature range over which the system remains stable.

To further ascertain the kinetic stability of the recovered polymer, we performed two-phase simulations where 624-atom simulation cells were filled with 192 atoms of the gaseous m_g phase and 432 atoms of the recovered polymeric $p_{a,rc}$ phase. A NVT-AIMD simulation was thereafter run for the two-phase mixture at 300 K for a total simulation time of 8.8 ps (the system

is well-equilibrated by 3.1 ps), equilibrating to a near-ambient pressure of 1.6 ± 0.6 kbar. As can be seen in Fig. 3a,b, there is coalescence of the polymeric chains with the gaseous mixture during the simulation. However, from the radial distribution function, $g(r)$, shown in Fig. 3c it is evident that the gaseous and amorphous parts of the mixture remain intact. The first peak of the $g(r)$, bifurcated at 1.16 Å and 1.25 Å, corresponds to the original molecular gaseous phase and changes insignificantly, with a slight reduction in the second peak due to the coalescence described earlier. The small features between 1.3 Å and 2.8 Å, which are signatures of the polymeric structure, remain unchanged during the simulations.

It can be argued that a <10-ps simulation using a few hundred atoms may not be a correct representation of reality, even for predictive purposes. Hence, we resorted to machine learned molecular dynamics (MLMD), using a machine learned interatomic potential (MLIP), for a 15,600-atom two-phase cell over 100 ns. This included 4,800 atoms in gas molecules and 10,800 atoms in amorphous structures. As can be seen in Figs. 3e and 3f, the gas phase molecules and $p_{a,rc}$ structure coexist without loss of kinetic stability for 100 ns, as demonstrated by the qualitatively unchanged radial distribution function. A more intuitive picture is presented through the mean square displacement (MSD) of different types of atoms. Amorphous chain/ring C,O atoms are locked into the structure; bulk gas as well as interfacial C,O drifts slowly until equilibrating at ~20 ns; the trapped O₂, as discussed earlier in Fig. 2, diffuses out of the amorphous structure without affecting the kinetic stability of the amorphous structure. The system equilibrates to a pressure of 1.9 ± 0.3 kbar, signifying near-ambient multi-ns stability of the two-phase system. The validity of the MLMD simulations rest on the accuracy of the MLIPs, as shown in terms of the root mean square error (RMSE) in energies and forces in Fig. 3i, but can also be further ascertained by the comparison of the vibrational density of states (VDOS) across different timescales. The torsional and bond-bending modes and their distribution remain fundamentally unchanged across ps-to-ns timescales, but there exists a shuffling among the layer and bond-stretch modes. This can, intuitively, be attributed to the release of the trapped O₂ inducing more breathing vibrational modes into the system. This relaxes any local layer-like characteristics and allows more lateral stretching in the amorphous network.

These results confirm the mechanical as well as kinetic stability of the polymeric phase at 300 K and a near-ambient pressure, with the highest temperature of stability being 700 K, when partial breakdown of the polymeric chain starts (discussed later).

Stability comparison with respect to compression and recovery of initially molecular carbon dioxide

Validating and understanding our theoretical findings for the polymerization of CO+O₂ requires an apt comparison with that of the well-studied CO₂ system. In this section, we examine comparatively the metastability of the two systems. For the latter, we consider three cases - crystalline CO₂-V ($P2_12_12_1$) and two amorphous solids generated as described below.

CO₂-V, as alluded to earlier, is the only polymeric carbon dioxide phase which has been recovered to ambient conditions, but only at temperatures below 200 K⁴⁵. Because single-phase AIMD simulations usually cannot capture crystalline transitions, due to simulation cell size and time constraints, we have used the experimental $P2_12_12_1$ structure as our starting point¹⁶. After equilibrating this structure at 60 GPa and 100 K, we decompressed it along the 100 K isotherm. However, at 4.9 ± 0.2 kbar, when increasing the temperature to only 200 K, this crystalline phase breaks down to gaseous CO₂ (see Supplementary Fig. S6) in complete agreement with the experimental results.

Next, we generated amorphous a -CO₂ similarly to the way it was synthesized experimentally. For this purpose, 144-atom simulation cells with gaseous CO₂ were heated to high temperature at ambient pressure using a NVT ensemble (to overcome kinetic reaction barrier) and subsequently compressed to pressures in the span of ~60 to ~118 GPa to overcome barriers for complete polymerization. After polymerization, they were slowly quenched to 300 K or below. For example, at ~60 GPa, a kinetic barrier of roughly 600 K has to be overcome in order to obtain an amorphous structure on quenching to 300 K. This kinetic barrier is inversely proportional to the pressure, and the barrier becomes only 300 K at ~118 GPa. The resulting a -CO₂ obtained this way is a mixture of three- and four-coordinated carbon atoms. It can be recovered to ambient conditions only along the 200 K or lower temperature isotherm and breaks down to gaseous CO₂ when heated up (in single-phase NVT -AIMD) to 300 K at 8.2 ± 0.2 kbar (see Supplementary Fig. S7). When decompressed along the 300 K isotherm, it breaks down to a molecular phase below ~30 GPa.

Finally, for a direct comparison with the polymerized CO and O₂ mixture (referred to as $p_{a,rc}[\text{CO}+\text{O}_2]$ here and in the following section for clarity), we obtained polymeric p -CO₂ (referred to as $p_{a,rc}[\text{CO}_2]$ in this section) directly by isothermal compression of 144-atom CO₂ simulation cells along the 300 K isotherm. A polymeric phase emerges beyond ~118 GPa comprised of entirely 4-coordinated carbon atoms. This is, in fact, the limiting case of a -CO₂, as mentioned in the previous paragraph. As pressure is reduced, $p_{a,rc}[\text{CO}_2]$ gradually changes from a fully four-coordinated to a mostly three-coordinated structure. Upon isothermal decompression to 6.2 ± 0.2 kbar at 300 K, this polymeric phase persists but breaks down to gaseous CO₂ at temperature at or above 400 K in single-phase NVT -AIMD simulations (see Supplementary Fig. S8).

Among the three aforementioned cases, only the latter yields a polymeric structure at ambient conditions. However, its stability is still significantly lower than that of $p_{a,rc}[\text{CO}+\text{O}_2]$, which persists at temperatures of at least 1000 K when heated at 7.7 ± 0.3 kbar (see Supplementary Fig. 8) as well as at ~29 GPa (see Supplementary Fig. S9) in single-phase simulations.

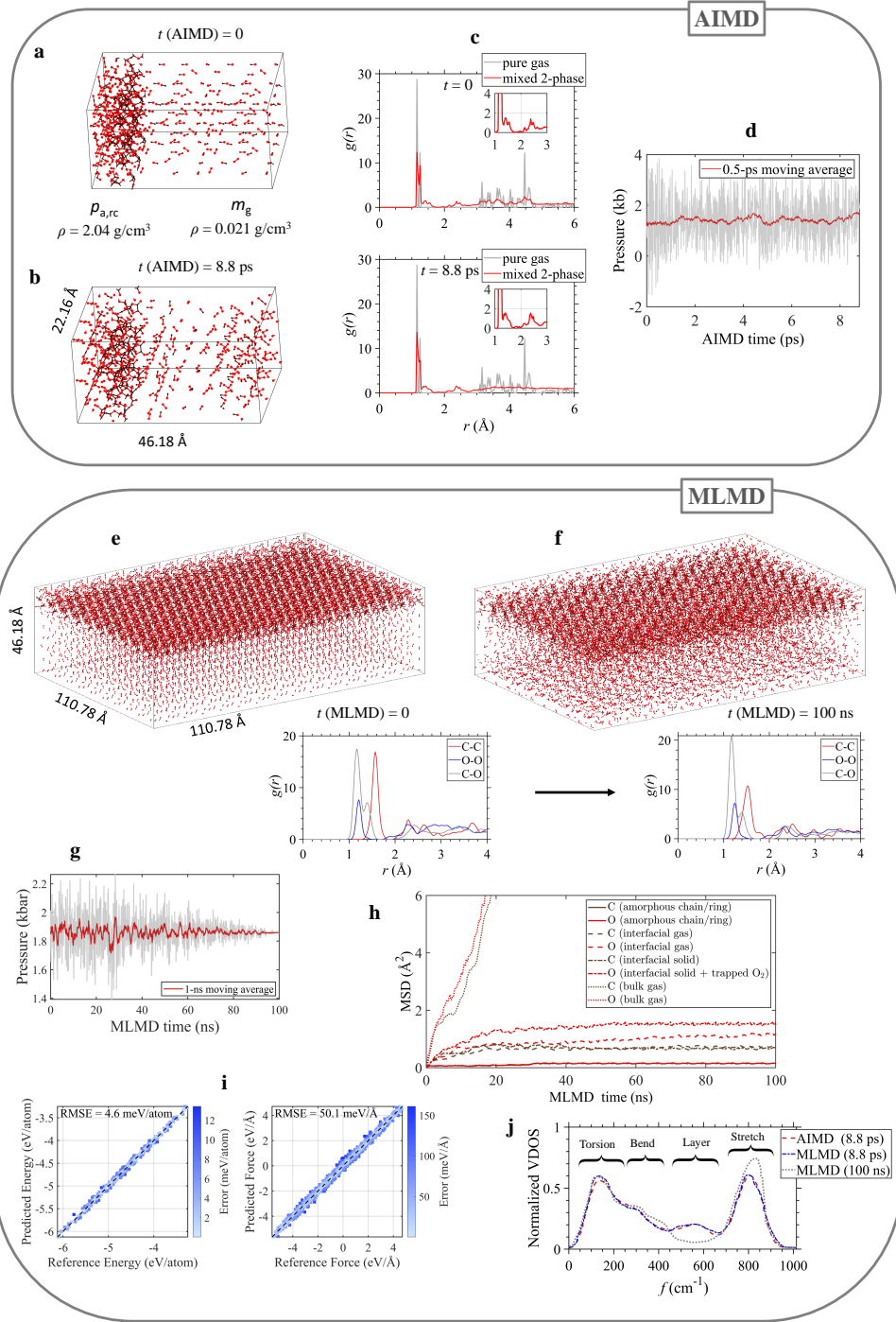


Fig. 3 Two-phase AIMD and MLMD results for the stability of polymeric amorphous material $p_{a,rc}$. Visualization of the **a** initial and **b** final atomic configurations along a 624-atom two-phase simulation trajectory (432 atoms initially in $p_{a,rc}$ and 192 atoms in m_g) at $P = 1.6 \pm 0.6$ kbar and $T = 300$ K. Oxygen and carbon atoms are shown in red and brown, respectively. **c** Radial distribution function, $g(r)$, for the initial (top) and final (bottom) configurations. The latter is averaged over simulation time of 5.7 ps, after equilibrating for over 3.1 ps. The insets show the polymeric $g(r)$ features that do not alter significantly during the course of the simulation. **d** Computed pressure during the AIMD simulation run is shown to remain at 1.6 ± 0.6 kbar. **e,f** The 15,600-atom MLMD configurations at **e** initial and **f** final (100 ns), and the associated radial distribution functions $g(r)$, demonstrating the stability of the recovered amorphous structure at larger length and time scales. **g** Computed pressure during the MLMD simulation run is shown to equilibrate at a value of 1.9 ± 0.3 kbar. **h** The polymeric amorphous phase stability is quantitatively shown by evolution of mean square displacement as a function of MLMD simulation time. **i** Parity plots of energy and forces for the machine learned interatomic potential (MLIP) with RMSE values mentioned. **j** Normalized vibrational density of states (VDOS) for AIMD (over 8.8 ps), MLMD (over first 8.8 ps), and MLMD (over entire 100 ns) are shown.

However, single-phase (heat-until-breakdown) simulations may overestimate the stability of the simulated phase. To determine more accurately the temperatures at which the polymeric phases break down, we carried out two-phase MLMD simulations for 11,520-atom two-phase cells, composed of the polymeric amorphous $p_{a,rc}$ and gaseous, molecular m -CO₂. As shown in Fig. 4, the structure remains intact at 500 K. However, on heating to 700 K, complete breakdown occurs, as evidenced by the broadening of the C-O radial distribution function.

In addition, NPT AIMD simulations for the $p_{a,rc}$ [CO+O₂] was also performed. Here, the target pressure was set at 1 kbar instead of 1 atm because fluctuations in the barostat yield transient negative normal stress components at such low pressures. Under these conditions, it was observed that $p_{a,rc}$ [CO₂] breaks down to a gaseous molecular form at just 300 K and 3.2 ± 0.1 kbar (see Supplementary Fig. S10), while $p_{a,rc}$ [CO+O₂] remains stable up to 700 K at 4.7 ± 0.2 kbar (see Supplementary Fig. S11 and S12), at which point it finally starts to break down partially.

In either of the above cases, whether the amorphous system is in contact with CO₂ or CO+O₂, the decomposition initiates only at 700 K. It should be noted that decomposition to CO₂ is the natural consequence because of the stability of m -CO₂.

Thus, our results predict that compressing CO+O₂ rather than CO₂ not only leads to polymerization at lower pressures but also results in a polymer that is significantly more stable upon pressure release. Note that during AIMD simulations, negative (tensile) normal stress components along any of the axes can lead to *unphysical* fragmentation of the polymers. The simulations were thus equilibrated at a kilobar of pressure. However, the PBE exchange-correlation functional tends to overestimate the pressure for the polymeric phases (discussed in the 'Energetics' section later). Therefore, these results can be used to ascertain the physics at ambient pressure.

Structural properties

The stability of polymers is directly linked to their atomic arrangements. To understand the differences among the recovered $p_{a,rc}$ [CO+O₂] and $p_{a,rc}$ [CO₂] phases, we therefore present a comparative analysis of their structural properties.

A qualitative comparison of radial distribution functions in Fig. 5a shows that the $p_{a,rc}$ [CO₂] structure is only centered around C–O bonds. In contrast, $p_{a,rc}$ [CO+O₂] has C–O, C=O, C–C, and O–O bonds, all contributing to the formation of chain-ring structures. Ball-and-stick models for the predicted chain or chain-ring structures are shown in Fig. 5b. The chain-ring structure in $p_{a,rc}$ [CO+O₂] is quite nuanced, with 5-member rings linked into the –O(CO)– chains (shown as 5_l), 5-member rings networked into a cage-type bonding mesh (shown as 5_n), and 6-member rings interlocked with 5-member rings (shown as 6_l). In contrast, the structure of $p_{a,rc}$ [CO₂] is just –O(CO)– chains.

The partial crystal order Hamiltonian population (pCOHP)^{47–49} analysis of the recovered $p_{a,rc}$ [CO+O₂] phase, shown for C-centered and O-centered bonds in Fig. 5c, shows the usual C–O and O–O (single) σ - σ^* bonding-antibonding orbital combinations and the O=C (double) π - π^* combination. Of significance here are the unusually strong C=C π - π^* bonds ($\Delta E \sim 16$ eV) and C–C σ - σ^* bonds ($\Delta E \sim 13$ eV). The C=C π - π^* bonds originate in the 6-member rings, which themselves are a result of including London dispersion forces in the simulations, while the C–C σ - σ^* bonds are present in the 5-member rings. Recall that at ambient conditions, all stable molecules formed from elements in the second row of the periodic table have stronger σ than π bonds. The absence of these bonds in $p_{a,rc}$ [CO₂] (evident from the $g(r)$ in Fig. 5a) may be a contributing factor in its reduced kinetic stability during decompression.

Another important parameter when analyzing pressure-induced structures such as $p_{a,rc}$ [CO+O₂] is the bond order. For synthesizing energetic materials using a compression-decompression method, ideally, we would want a transition similar to the formation of cg -N, where all triple bonds delocalize into single bonds. The integrated COHP (ICOHP) versus the bond order of $p_{a,rc}$ [CO+O₂] as a function of pressure is shown in Fig. 5c, the bond order being calculated using the integrated crystal order bond index (ICOBI) analysis^{49,50}. As the pressure increases from 15 GPa to 31 GPa, the value of the *maximum* bond order reduces from ~ 3 to ~ 2 , indicating that the system is evolving towards a higher energetic state.

A distribution of the nearest-neighbor coordination numbers (NNCN) for the C–O, O–C, O–O, and C–C pairs in $p_{a,rc}$ [CO+O₂] and $p_{a,rc}$ [CO₂] is shown in Fig. 5d, with their mean values summarized in Table 1. The main observation here is the near absence of C–C and O–O bonding in $p_{a,rc}$ [CO₂]. The average C–O NNCN of ~ 3 , alongside O–C NNCNs of 1 and 2, also suggests the abundance of three-coordinated –O(CO)– chains in that structure, which is in clear contrast to $p_{a,rc}$ [CO+O₂], where the chain intermittently has 5- and 6-member rings, thereby decreasing the mean C–O NNCN. The crystalline CO₂-V ($P2_12_12_1$) phase, recovered to ambient pressure and 100 K, is also included in the table, again showing a complete absence of C–C bonding. It is important to note the existence of O–O pairs in both recovered systems, as mentioned earlier for the CO+O₂ case. Their implications will be discussed later in the section on chemical dynamics.

In summary, the compression of a CO and O₂ mixture leads to the formation of a drastically different high-pressure structure compared to that of compressed CO₂. The structural differences manifest in increased metastability of the polymerized amorphous product when it is recovered to ambient pressure.

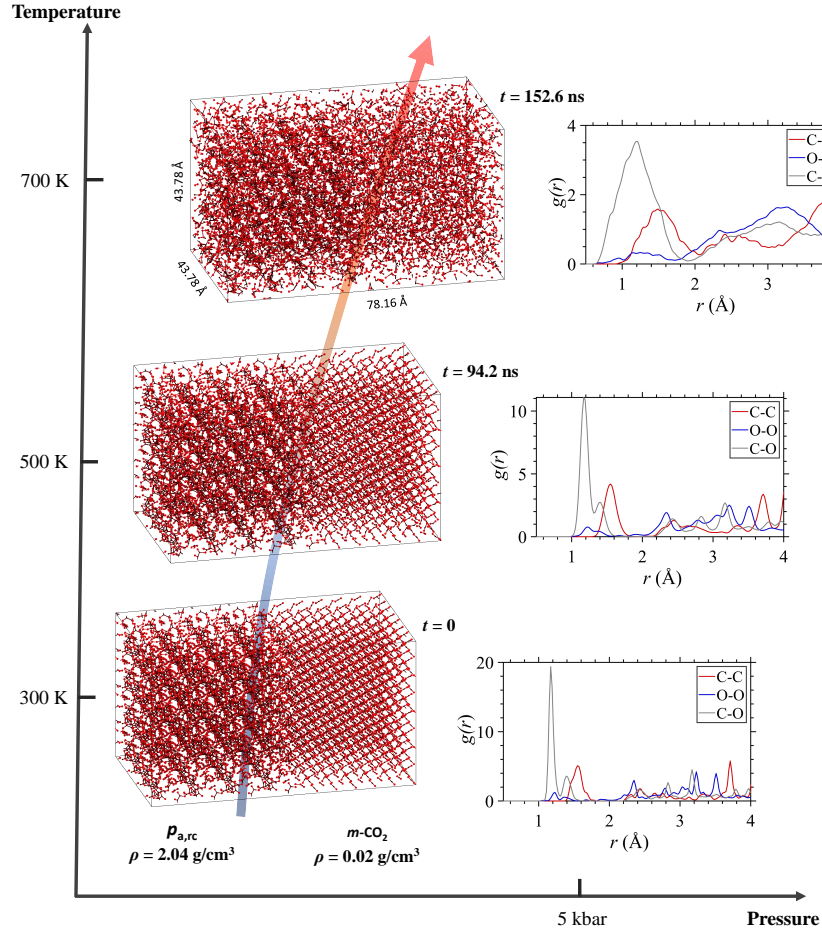


Fig. 4 Kinetic stability of the polymeric amorphous $p_{a,rc}$ phase checked using 11,520-atom two-phase simulations ($p_{a,rc}$ in one side and gaseous, molecular $m\text{-CO}_2$ in the other) by heating the two-phase cell to 500 and 700 K, over a total simulation time of 152.6 ns. The polymeric amorphous phase starts decomposing at 700 K, as seen in the topmost radial distribution function.

Table 1 Values of mean Nearest Neighbor Coordination Number (NNCN) calculated for different ion-type pairs in recovered phases of $p_{a,rc}[\text{CO}_2]$ at 200 K, $p_{a,rc}[\text{CO}+\text{O}_2]$ at 300 K, and $\text{CO}_2\text{-V}$ at 100 K.

Mean NNCN	$p_{a,rc}[\text{CO}_2]$	$p_{a,rc}[\text{CO}+\text{O}_2]$	$\text{CO}_2\text{-V}$
Carbon-Oxygen	3.08	1.85	3.93
Oxygen-Carbon	1.78	0.92	1.95
Oxygen-Oxygen	0.32	0.21	0.00
Carbon-Carbon	0.08	1.37	0.00

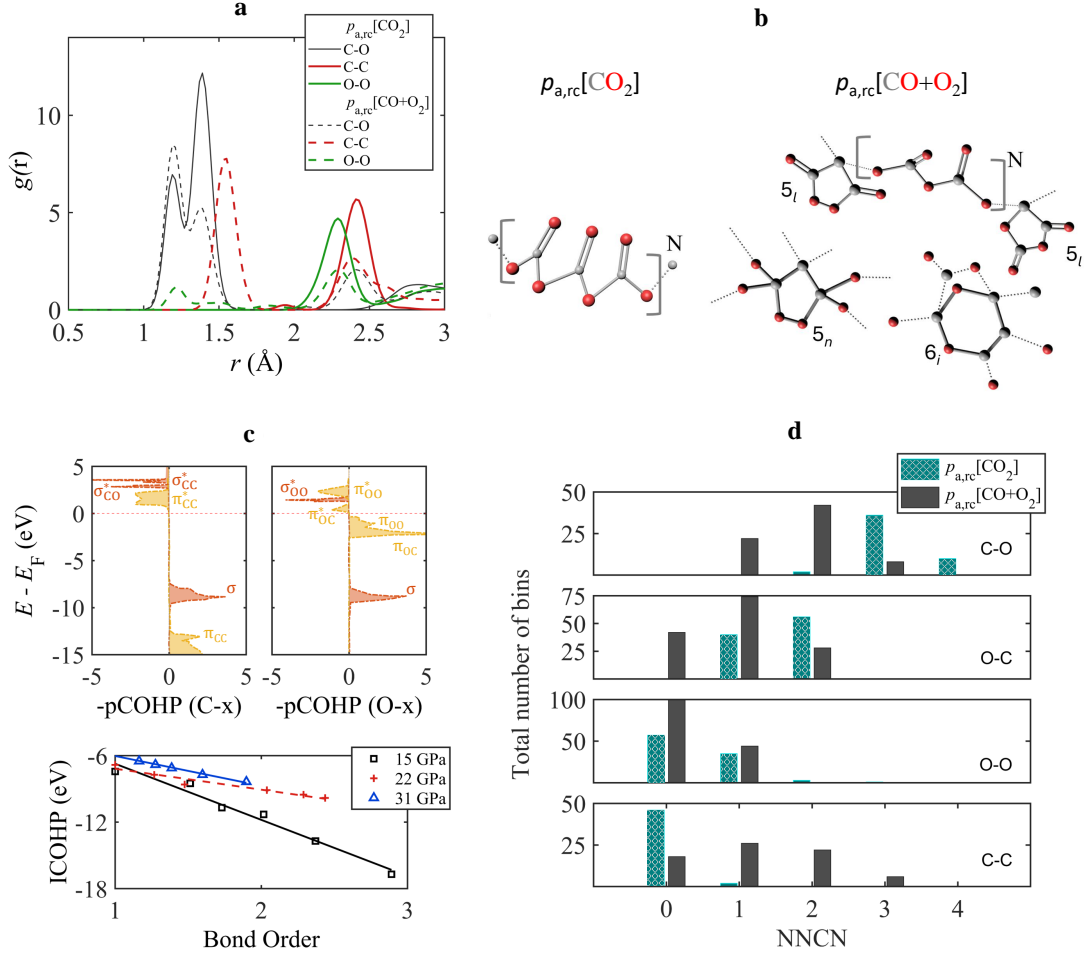


Fig. 5 Comparative analysis of the structural features of the recovered polymeric phases of CO_2 ($p_{a,rc}[\text{CO}_2]$ at 200 K) and $\text{CO}+\text{O}_2$ ($p_{a,rc}[\text{CO}+\text{O}_2]$ at 300 K). **a** Pairwise radial distribution function, $g(r)$, for both systems at near-ambient pressures. **b** Comparison of chain structures, with carbon and oxygen atoms shown in grey and red, respectively. Here, 5_l , 5_n , and 6_i indicate 5-member chain-linked, 5-member networked, and 6-member interlocked rings, respectively. **c** Partial crystal orbital Hamiltonian population (pCOHP) for $p_{a,rc}[\text{CO}+\text{O}_2]$ for C-centered (top-left) and O-centered (top-right) bondings, as well as the integrated COHP as a function of bond order for selected pressures. **d** Nearest neighbor coordination number (NNCN) histograms for C–O, O–C, O–O, and C–C pairs.

Table 2 Interpolated values of enthalpy of formation ($\Delta_f H$), density (ρ_{rc}) and volumetric energy density (E_v) for the decompressed/recovered polymeric CO+O₂ phase $p_{a,rc}$, where $\Delta_f H$ has been calculated with respect to gaseous molecular CO₂ at ambient as detailed in Supplementary Tables S3, S4 and S5 of Supplementary Discussion 6

Exchange-Correlation used	$H_{p_{a,rc}}$ (eV/CO ₂)	$\Delta_f H$ (kJ/mol)	ρ_{rc} (g/cc)	E_v (kJ/cc)
PBE (AIMD)	-20.707	-222.173	1.615	8.153
PBE + D3[0] (AIMD)	-17.711	-209.343	2.042	9.713
SCAN-L + rVV10 (AIMD)	-24.109	-207.484	2.281	10.754
SCAN + rVV10 (static)	-23.733	-204.325	2.348	10.901
HSE06 (static)	-25.909	-243.206	2.338	12.920

Energetics

The potential use of $p_{a,rc}[\text{CO}+\text{O}_2]$ as an energetic material depends on the density of the recovered phase and its energy relative to the thermodynamically stable phase at ambient conditions, namely, molecular CO₂. In this section, we focus on computing these properties.

For a more detailed look at the energetics of the systems under consideration, we went beyond the PBE (GGA) exchange-correlation functional. In order to estimate the formation enthalpy of the final polymerized product more accurately, *NVT*-AIMD simulations were performed for the full compression-decompression trajectories with PBE⁵¹, PBE + D3[BJ]⁵², PBE + D3[0]⁴⁶, PBE + rVV10^{53,54}, and SCAN-L⁵⁵ + rVV10 combinations. Cell sizes with 432 and 864 atoms were used for the PBE and 258 atoms for the SCAN-L AIMDs (summarized in Supplementary Table 1). In addition, static single-point calculations were performed on five to seven configurations at each density along the PBE-calculated isothermal 108-atom AIMD trajectory using SCAN⁵⁶, SCAN + rVV10 and HSE06⁵⁷ functionals, and then averaged. Fermi-Dirac smearing corresponding to a temperature of 300 K was used for these calculations.

The pressure-density equations of state (EOS) for the CO+O₂ system are shown in Fig. 6a, calculated using the different combinations of exchange-correlation functions, van der Waals treatment and cell sizes (see Figs. S13 to S17 for a broader version). The kinks in the EOS curves coincide with the initialization of $-\text{C}-\text{C}-$ polymerization. There is a general downward revision of pressure for the same density for SCAN-L and HSE06 w.r.t. PBE calculations, similar to observations of Bonev *et al.*³³ on CO simulations for HSE06 w.r.t. PBE.

The ranges of pressure over which $-\text{C}-\text{C}-$ and $-\text{C}-\text{O}-$ bonds and rings form are shown in Fig. 6b for the different combinations of cell size, exchange-correlation functional, and van der Waals treatment used. It can be seen that the polymerization process is delayed when using meta-GGA, but the behavior of sequential bond formation remains consistent. With respect to the PBE + D3[0] 864-atom simulations, which form the bulwark of the analyses in this paper, the pressure domains for $-\text{C}-\text{C}-$, $-\text{C}-\text{O}-$ and rings are ~ 7.1 -8.5 GPa, ~ 12.2 -13.2 GPa, and ~ 19.3 -23.2 GPa, respectively.

Figure 6 shows the equations of state for the compression-decompression cycle of the CO+O₂ system from *NVT*-AIMD simulations using an 864-atom cell, alongside the same cycle for 144-atom CO₂ cells at 200 K, all within PBE + D3[0]. The CO₂ system ends with an enthalpy higher than its starting molecular state, which is expected because molecular CO₂ is the most stable form at ambient pressure. A similar curve for the polymeric crystalline $p_{c2}[\text{CO}+\text{O}_2]$ system (obtained from metadynamics) was also evaluated, where it was decompressed to ambient conditions using *NVT*-AIMD simulations in a 288-atom cell. However, this crystalline phase breaks down into the constituent CO and O₂ molecules below a pressure of ~ 9 GPa and a density of ~ 1.7 g/cc. This confirms that only the amorphous polymeric phase of CO+O₂ is recoverable.

The comparative analysis of density values, in Table 2, shows a compression of an initial gaseous mixture (m_g) with a density of 0.021 g/cc to a recovered polymer ($p_{a,rc}$) with density of 2.04 g/cc within PBE + D3[0]; this can be as high as 2.28 to 2.34 g/cc with corrections using meta-GGA or hybrid functionals. It is important to mention here that the deviation in the calculated values for the mass density and volumetric energy density is approximately 41% and 32%, respectively, although the gravimetric energy density varies only by 7%. The formation enthalpy of ~ 204 -243 kJ/mol (~ 4.6 -5.5 kJ/g) is more than that of CO, which stands at ~ 95 kJ/mol (~ 3.4 kJ/g)³³, i.e., more stable. Furthermore, unlike CO, this composition is not susceptible to decomposition to graphite and oxygen, but converts to lower energy molecular CO₂ at a sufficiently high $T > 500$ K. In essence, the process ends up yielding a denser polymer both gravimetrically and energetically.

In terms of comparison to carbon dioxide, also shown in Fig. 7, the recovered $p_{a,rc}[\text{CO}_2]$ differs from the recovered $p_{a,rc}[\text{CO}+\text{O}_2]$ with a density higher by ~ 0.1 g/cc and an enthalpy lower by ~ 1 eV/CO₂ molecule. This suggests that for near-similar quantitative bulk properties of the recovered amorphous phase, a significant reduction in polymerization onset pressure has been achieved.

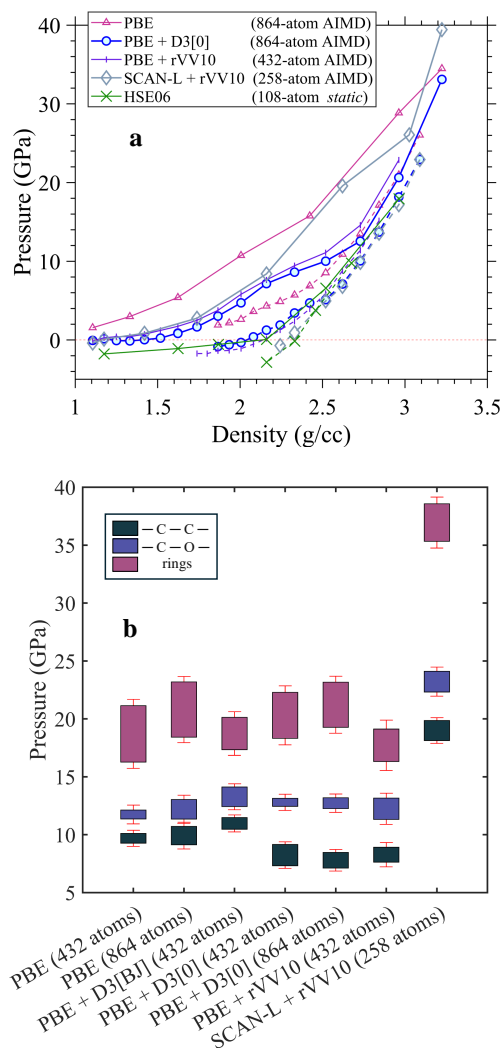


Fig. 6 **a** Equations of state along the compression-decompression paths of CO+O₂ obtained within *NVT*-AIMD at $T=300$ K using various combinations of cell sizes, exchange-correlation functionals and van der Waals treatment. Solid and dashed lines indicate compression and decompression paths, respectively. **b** Pressure ranges over which the formation of —C—C— and —C—O— bonds and rings are observed under different simulation parameters. The red error bars are the standard deviations of the pressures in the ensemble-averaged *NVT*-AIMD simulations.

Phenomenological analysis of chemical dynamics

To understand the formation of the p_a phase and its structural differences from the polymeric CO₂ phases, we analyze the atomic dynamics within the CO+O₂ and CO₂ systems before and after the onset of polymerization. We define the atomic number density, $\rho_N(r)$, as the number of atoms within a sphere of radius r centered on an atom, averaged over all atoms and configurations in the AIMD. This density exhibits a wavy profile close to the onset of polymerization. The sphere around each atom, inside which the first monomers starts forming, has a radius equal to the first minimum of $\rho_N(r)$ and is called the kinetic sphere of radius R_{ks} .

The evolution of the atomic arrangement in CO+O₂ along a compression trajectory – from a nearly homogeneous molecular

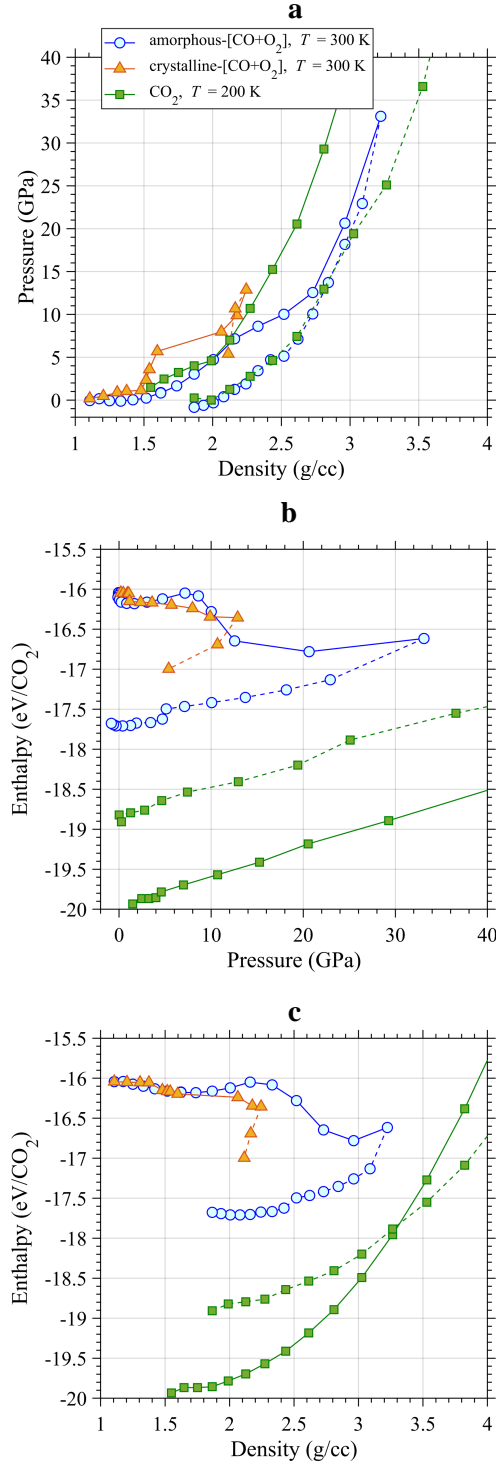


Fig. 7 Equations of state along the compression-decompression paths of the amorphous $p_{a,rc}[\text{CO}+\text{O}_2]$ obtained using NVT -AIMD at $T=300$ K, the polymeric crystalline $p_{c2}[\text{CO}+\text{O}_2]$ obtained with metadynamics along the compression path and subsequently decompressed using NVT -AIMD at $T=300$ K, and the compound CO_2 obtained with NVT -AIMD at $T=200$ K are presented in **a** pressure-density, **b** enthalpy-pressure, and **c** enthalpy-density spaces. The solid and dashed lines represent the compression and decompression paths, respectively. All curves are evaluated within PBE + D3[0], using 432-atom, 288-atom, and 144-atom simulation cells for amorphous $\text{CO}+\text{O}_2$, crystalline $\text{CO}+\text{O}_2$, and CO_2 , respectively. The curves corresponding to $\text{CO}+\text{O}_2$ in Fig. 6a are the same as the PBE + D3[0] data shown in Fig. 1b. The data for CO_2 is only shown up to 40 GPa, while the polymerization of this system commences beyond ~ 118 GPa at 300 K.

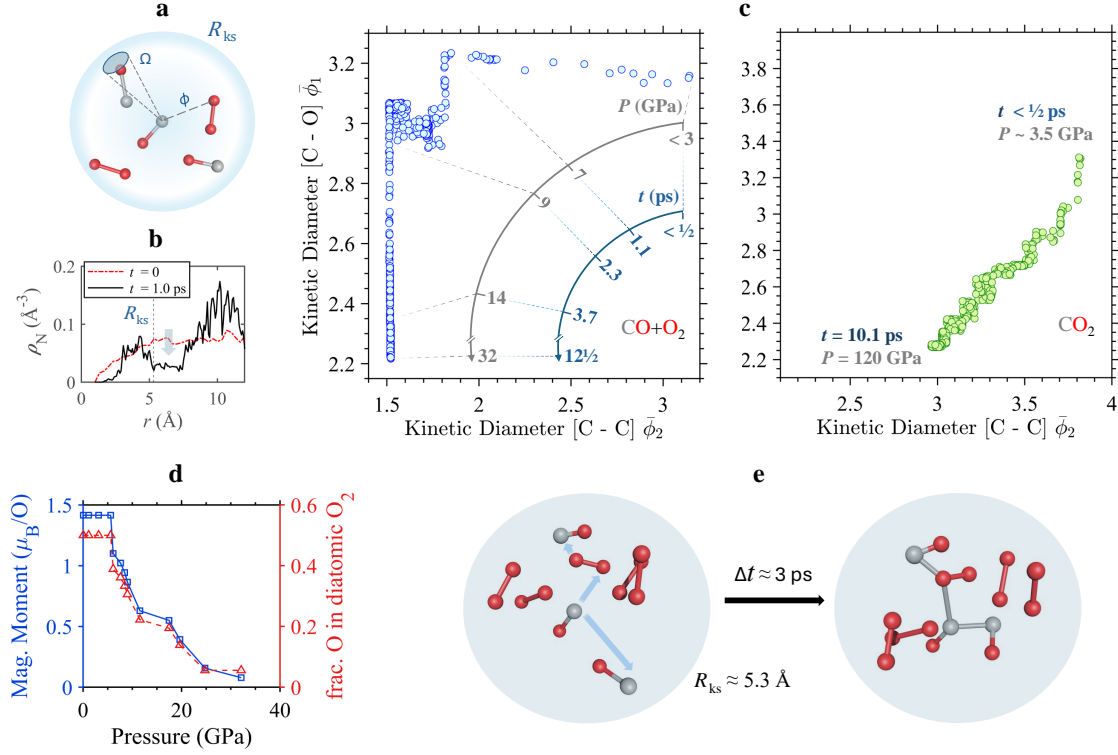


Fig. 8 **a** An illustration of kinetic sphere of radius R_{ks} (shaded as a blue circle) and kinetic diameter ϕ defined in the text. **b** Radial number density, ρ_N , for the CO+O₂ system at ambient pressure ($t = 0$) and the onset of polymerization ($t = 1.0$ ps) along a compression trajectory. **c** Evolution of the kinetic [C–O] $\bar{\phi}_1$ versus [C–C] $\bar{\phi}_2$ diameters along isothermal compression simulations starting from ambient pressure at 300 K. The CO+O₂ and CO₂ systems are compressed up to 32 and 120 GPa, respectively. The two radial axes for CO+O₂ show the time and pressure for specific points of significance along the AIMD trajectory. **c** Change in average magnetic moment per oxygen atom and fraction of residual molecular O₂ as a function of pressure. **d** Atomic arrangements from an AIMD trajectory showing the relative arrangements of CO and O₂ molecules in the vicinity of O₄ clusters, together forming the kinetic sphere.

system at $t = 0$ (ambient pressure) to an aggregated one with $R_{ks} = 5.3$ Å at $t = 1$ ps ($P \sim 7$ GPa) – is illustrated in Fig. 8b. Since R_{ks} is easily discernible only in the density region where the polymerization occurs, we define R_{ks} along the entire compression trajectory as:

$$R_{ks} = \begin{cases} R_{ks}(t') \times l(t)/l(t') & t \leq t' \\ R_{ks}(t) & t'' > t > t' \\ R_{ks}(t'') \times l(t)/l(t'') & t \geq t'' \end{cases} \quad (1)$$

Here t is the simulation time along the compression trajectory (corresponding to a specific density/pressure), t' and t'' are the times where the polymerization commences and ends, and $l(t)$ is the dimension of the cubic simulation box. The exact values of t' and t'' are not critical for the analysis.

The mean distance between atoms X (where X is C or O) with all the first-neighboring Y atoms (C or O) inside their kinetic spheres, sans the Y atom in its own molecule, is the X–Y kinetic diameter $\bar{\phi}_1$:

$$\bar{\phi}_1 = \frac{1}{N_X} \sum_{i=1}^{N_X} \sum_{j=1}^{N_{Y,ks(i)}} \frac{\phi_{ij}}{N_{ks,Y}(i)}, \quad (2)$$

where N_X is the total number of X atoms in the cell and $N_{Y,ks}(i)$ is the total number of first-neighbor Y atoms inside the kinetic sphere of the i^{th} X atom, but not bonded with it. During this computation, we ensure that the following condition is satisfied:

$$\sum_{j=1}^{N_{O,ks}(i)} 2\pi(1 - \cos\Omega_j) \lesssim 4\pi, \quad (3)$$

where $\Omega_j = [\cos^{-1}(\phi_j/r_{shell})]$ is the subtended solid angle of the j^{th} Y atom with respect to a shell of radius r_{shell} . Here the radial distance between the n^{th} and $n+1^{th}$ shells calculated radially outwards from the X atoms, $\Delta r_{shell} [= r_{shell,n+1} - r_{shell,n}]$, is the tunable parameter used to ensure that the total subtended solid angle is approximately equal to 4π sr.

The evolution of the C–O versus C–C kinetic diameters along an 864-atom AIMD compression trajectory spanning pressures from ambient to ~ 32 GPa during a 12.5 ps simulation are shown in Fig. 8c. Here t' and t'' are estimated at 0.5 ps and 7.6 ps, respectively, for the CO+O₂ system. The resulting locus of points exhibits a Γ -shaped path. Note that a similar observation holds true even if just the nearest or the average of the first two to five neighboring atoms is used to define ϕ (see Supplementary Figure S18).

The C–C polymerization happens just beyond ~ 7 GPa, which corresponds to the corner of this Γ -shaped path, where ϕ_2 is minimized; presumably the system overcomes the activation barrier for polymerization. Thereafter, as the C–C polymerization completes by ~ 9 GPa, relaxation of ϕ_1 is observed, most likely an effect of C–O polymerization which completes by ~ 14 GPa. The cumulative simulation time needed for these two stages of polymerization is approximately 3 ps, which gives us a benchmark for the time scales of bond rearrangement in such compressed carbon-oxygen systems. This is comparable to the experimentally observed timescales of 1-3 ps in both ionic as well as cyclic covalent compounds^{58–60}.

In the case of CO₂, a Γ -shaped path is not followed by the kinetic diameters, despite a simulation time of 10 ps, even though the system eventually reaches a four-coordinated amorphous structure. This highlights the fact that, although the CO + O₂ mixture and CO₂ are stoichiometrically equivalent, the dynamics of their reaction trajectories are completely different. The linear O=C=O molecules impose geometrical constraints on their approach to one another that are not present in the CO + O₂ mixture, thereby inhibiting C–C bond formation.

Another interesting observation is the local reaction environment inside the simulation cell. In a 2:1 CO:O₂ mixture, the residual magnetic moment of oxygen in the cell is shown in Fig. 7d as a function of pressure. The average magnetic moment is $1.41 \mu_B$ at ambient and decreases with increasing pressure. This is consistent with an ample amount of free O₂ molecules in the CO+O₂ cell at lower pressures, including conditions where –C–C– and –C–O– bonds form. To visualize the effect of the residual O₂, we look inside a kinetic sphere during a simulation. As shown in Fig. 7e, O₂ molecules tend to aggregate into O₄ clusters, which is similar to the ϵ phase of oxygen at comparable pressures^{61,62}. They provide a local potential energy environment within which CO and other O₂ molecules react to form –C–C– and –C–O– bonds. The elimination of such an environment, akin to the case of undersaturation in Fig. 2a, inhibits polymerization. This shows that even though the mixture is stoichiometrically equivalent to the compound CO₂, the local chemical environment during polymerization is completely non-stoichiometric.

Discussion

Density functional theory-based methods were employed to predict a novel, low-pressure pathway for synthesizing a metastable polymeric amorphous form of CO₂ that can be recovered at ambient conditions and functions as a high-energy-density material. Traditional routes to fully 4-coordinated polymeric CO₂ require extreme pressures (~ 118 GPa), and the resulting phases revert to molecular CO₂ upon decompression at room temperature. Here, we propose compressing a mixture of CO and O₂ (stoichiometrically equivalent to CO₂) along the 300 K isotherm, which lowers the polymerization onset to ~ 7 GPa and complete C–C polymerization by ~ 23 GPa — a significant reduction in required pressure. Upon decompression back to ambient pressure at 300 K, this polymeric phase remains intact with negligible changes in bonding statistics, evidencing mechanical as well as kinetic stability.

Constrained metadynamics searches identify two transient crystalline intermediates that are slightly favorable below 10 GPa but quickly amorphize under further compression, confirming that the amorphous phase is the predominant product at higher pressures. Importantly, small quantities of unreacted O₂ persist up to ~ 30 GPa, later forming oxygen chains that integrate into the polymer without disrupting its structure — an effect shown to enhance kinetic barriers and thus metastability.

Kinetic stability is further probed via two-phase AIMD (624 atoms) for >8 ps, and large-scale MLMD (15,600 atoms) for 100 ns. Both demonstrate coexistence of polymer and gas, stable pressures (1.6–1.9 kbar) at room temperature, and locked-in C,O frameworks, with unreacted O₂ diffusing out without collapsing the polymer. Phonon analyses confirm no imaginary modes, indicating mechanical metastability, while MLMD as well as two-phase *NPT* AIMD shows that the polymeric amorphous structure remains stable up to 700 K at near-ambient pressures before partial breakdown.

Structural comparisons between recovered polymeric-[CO+O₂] and conventional polymeric-[CO₂] reveal key differences: the former exhibits C–O, C=O, C–C, and O–O bonds forming complex chain-ring networks (with 5- and 6-member rings), whereas the latter comprises mainly three-coordinated -O(CO)- chains with minimal C–C or O–O bonding. Crystal Orbital Hamilton Population (COHP) analyses highlight unusually strong C=C π - π^* and C–C σ - σ^* interactions in polymeric-[CO+O₂], suggesting higher stored energy. Energetic metrics predict higher formation enthalpies (–204 to –243 kJ/mol), densities (2.04–2.34 g/cc), and volumetric energy densities (8.2–12.9 kJ/cc) - surpassing polymeric CO₂ and rivaling TNT energetics.

If the prediction that compression of an initial metastable mixture lowers the onset of polymerization and yields kinetically robust HED materials is generally true, then this opens up opportunities to create and recover various energetic materials starting from initial mixtures of C,H,O,N compounds as the starting building blocks. To this end, we have provided Raman signatures of the relevant polymeric and amorphous phases in Supplementary Discussion 8 for aiding in experimentation.

Methods

Ab initio one-phase simulations

Ab initio molecular dynamics (AIMD) simulations, utilizing the Born–Oppenheimer approximation⁶³, with temperature being controlled via a Nosé–Hoover thermostat in a canonical (constant-*NVT*) or an isothermal–isobaric (constant-*NPT*) ensemble, form the backbone of the methods used in this paper.

The Vienna *Ab Initio* Simulation Package (VASP)^{64–66} was used for such calculations, where 4- and 6-electron *hard* projector augmented wave (PAW) pseudopotentials were used for carbon and oxygen respectively, with a 850 eV plane-wave cutoff energy for generalized gradient approximation (GGA)⁶⁷ and 1000 eV for meta-GGA exchange-correlation functionals. Most of these calculations were performed using the Γ -point for sampling (resolution of at least $< 2\pi \times 0.10 \text{ \AA}^{-1}$) the first Brillouin zone (1BZ) but for some cases, we used a single special **k**-point (1/4, 1/4, 1/4), as was introduced by A. Baldereschi⁶⁸.

Supercells were used, with 108, 192, 216, 258, 432 and 864 atoms, with an ionic time step of 0.5–0.8 fs for AIMDs at ambient pressure and temperature. Cubic supercells were used to prevent a bias towards any non-amorphous structure. For equilibrating simulations along these compression and decompression paths, the combination of ionic step size and total number of steps was such that the total physical time for the simulation system was always more than 5 ps, exceeding 10 ps in pivotal cases (see Supplementary Table 1 and 2 for complete list).

Oxygen was considered to be magnetic in all production simulations (see Supplementary Table 1) by utilizing spin-polarized calculations. This allows the converged ground-state solution to be the triplet (total spin $S = 1$) state, rather than the singlet state⁶⁹.

The PBE (Perdew–Burke–Ernzerhof) formulation⁵¹ of the GGA exchange-correlation functional was mostly used for the simulations. However, to check for the effects of climbing up Jacob’s ladder, as the sensitivity of reaction kinetic barriers to the nature of exchange-correlation is of utmost importance^{70,71}, the SCAN (strongly constrained and appropriately normed)⁵⁶ and SCAN-L⁵⁵ meta-GGA functionals were also used. The hybrid functional HSE06 (Heyd–Scuseria–Ernzerhof)⁵⁷ was also used for static tests. For van der Waals dispersion to be taken into account, the DFT-D3 [zero damping]⁴⁶, DFT-D3 [Becke–Johnson damping]⁵², and the rVV10 (revised Vydrov–van Voorhis) non-local correlation functional^{53,54} were used. Thus, the combinations of PBE, PBE + D3[BJ], PBE + D3[0], PBE + rVV10, and SCAN-L + rVV10 were used for AIMD simulations, while PBE, SCAN, SCAN + rVV10 and HSE06 were used for single-point calculations at multiple snapshots along the compression and decompression AIMD trajectories.

The compression and decompression analysis of any system using *NVT*-AIMD simulations, starting with a gaseous mixture configuration at < 0.1 kbar, involved a two-step approach. First, a *fast compression* trajectory was simulated using short simulations of 500 ionic steps at each volume along an isotherm, starting from ambient conditions. The volume was *decreased* by 1–2% at each point on the trajectory. Upon reaching the furthest point along the isotherm where complete pressure-induced polymerization is observed, equilibration simulations were performed for 5–10 ps, as described earlier (see Supplementary Table 1), at this furthest point as well as at intermediate points along the compression path for finding the resulting equilibrated ionic arrangement and constructing the equation of state. Second, for recovery, a *fast decompression* trajectory was similarly simulated with the volume being *increased* by 1–2% at each point on the trajectory. Equilibrating AIMD simulations of 5–10 ps were also performed at select points on the decompression trajectory to find the resulting equilibrated ionic arrangement and constructing the recovery equation of state.

Ab initio two-phase simulations

For the two-phase simulations, we performed a few cases with *NVT* ensemble while the rest were *NPT* ensemble simulations. In each of these cases, we started with cuboid supercells, with each side’s phase being well-equilibrated beforehand with respect to atomic arrangements using *NVT* simulations. The two-phase simulations used Baldereschi **k**-point for sampling, with 192 atoms for *m*-CO₂ | $p_{a,rc}$ [CO₂], and 216 to 624 atoms (see Supplementary Table 2) for *m*-[CO+O₂] | $p_{a,rc}$ [CO+O₂]

systems respectively. Here, the symbol $|$ is used to denote each of the two phases on either side. Then a AIMD simulation was performed on these merged cells with a time step of 0.5 fs, with a total simulation time exceeding 5 ps for all cases.

For the larger-scale 15,600-atom m -[CO+O₂] $|$ $p_{a,rc}$ [CO+O₂] and 11,520-atom m -CO₂ $|$ $p_{a,rc}$ [CO+O₂] two-phase *NVT* MLMD simulations, machine learned interatomic potentials (MLIPs) trained using Allegro^{72–74} was used to perform molecular dynamics simulations using LAMMPS⁷⁵. The training was performed within the RMSE threshold of 5 meV/atom for energies and 50 meV/Å for forces.

Metadynamics

Constrained *NPT*-metadynamics calculations were performed, with the PBE + D3[0] exchange-correlation functional and the bias potential being constructed of fixed Gaussians, at each p, T point after constraining the C–O and O–O bond lengths at higher pressures to within 2.5% of ambient values (as observed in AIMD at corresponding pressures) and using the cell basis vectors (magnitude as well as angles) as collective variables. Cell sizes corresponding to 36- to 108-atoms were used for the simulations, in increments of 6 atoms (i.e. 2CO+O₂). It is worth mentioning that, as a check, metadynamics simulations were also performed without constraining bond lengths, which yielded molecular crystal CO₂-I as the stable solution. This is unphysical given the fact that at 300 K, the system's thermal energy is insufficient for the reaction of CO and O₂, even at 30 GPa.

Vibrational spectra

Phonon and Raman spectra calculations were performed, in 108-atom cells with PBE + D3[0] functional, utilizing density functional perturbation theory (DFPT)⁷⁶ calculations for the Born effective charge (BEC) tensor and Phonopy⁷⁷ was utilized for evaluating the dynamical response of the system. Raman spectra was calculated (see Supplementary Discussion 8 for formulation) using this BEC tensor.

Input, configuration, and trajectory files for compression and decompression pathways have been uploaded at <https://doi.org/10.5281/zenodo.15027031> for the sake of repeatability.

References

- Novoselov, D. Y., Korotin, D. M., Shorikov, A. O., Oganov, A. R. & Anisimov, V. I. Weak Coulomb correlations stabilize the electride high-pressure phase of elemental calcium. *J. Physics: Condens. Matter* **32**, 445501 (2020).
- Ma, Y. *et al.* Transparent dense sodium. *Nature* **458**, 182–185 (2009).
- Neaton, J. & Ashcroft, N. Pairing in dense lithium. *Nature* **400**, 141–144 (1999).
- Hilleke, K. P., Bi, T. & Zurek, E. Materials under high pressure: a chemical perspective. *Appl. Phys. A* **128**, 441 (2022).
- Sundqvist, B. Carbon under pressure. *Phys. Reports* **909**, 1–73 (2021).
- Datchi, F., Dewaele, A., Le Godec, Y. & Loubeyre, P. Equation of state of cubic boron nitride at high pressures and temperatures. *Phys. Rev. B* **75**, 214104 (2007).
- Goncharov, A. F. *et al.* Thermal equation of state of cubic boron nitride: Implications for a high-temperature pressure scale. *Phys. Rev. B* **75**, 224114 (2007).
- Eremets, M. I., Gavriluk, A. G., Trojan, I. A., Dzivenko, D. A. & Boehler, R. Single-bonded cubic form of nitrogen. *Nat. Mater.* **3**, 558–563 (2004).
- Peiris, S. M. & Piermarini, G. J. *Static compression of energetic materials* (Springer, 2008).
- Xu, Y. *et al.* Free-standing cubic gauche nitrogen stable at 760 K under ambient pressure. *Sci. Adv.* **10**, eadq5299 (2024).
- Bini, R., Ulivi, L., Kreutz, J. & Jodl, H. J. High-pressure phases of solid nitrogen by Raman and infrared spectroscopy. *The J. Chem. Phys.* **112**, 8522–8529 (2000).
- Eremets, M. *et al.* Polymerization of nitrogen in sodium azide. *The J. Chem. Phys.* **120**, 10618–10623 (2004).
- Mattson, W. D., Sanchez-Portal, D., Chiesa, S. & Martin, R. M. Prediction of new phases of nitrogen at high pressure from first-principles simulations. *Phys. Rev. Lett.* **93**, 125501 (2004).
- Gregoryanz, E. *et al.* High P-T transformations of nitrogen to 170 GPa. *The J. Chem. Phys.* **126** (2007).
- Pickard, C. J. & Needs, R. High-pressure phases of nitrogen. *Phys. Rev. Lett.* **102**, 125702 (2009).
- Yoo, C. *et al.* Crystal structure of carbon dioxide at high pressure: “Superhard” polymeric carbon dioxide. *Phys. Rev. Lett.* **83**, 5527 (1999).

17. Bonev, S., Gygi, F., Ogitsu, T. & Galli, G. High-pressure molecular phases of solid carbon dioxide. *Phys. Rev. Lett.* **91**, 065501 (2003).
18. Giordano, V. M., Datchi, F. & Dewaele, A. Melting curve and fluid equation of state of carbon dioxide at high pressure and high temperature. *The J. Chem. Phys.* **125** (2006).
19. Santoro, M. *et al.* Amorphous silica-like carbon dioxide. *Nature* **441**, 857–860 (2006).
20. Giordano, V. M., Datchi, F., Saitta, A. M. & *et al.* Molecular carbon dioxide at high pressure and high temperature. *Europhys. Lett.* **77**, 46002 (2007).
21. Iota, V. *et al.* Six-fold coordinated carbon dioxide VI. *Nat. Mater.* **6**, 34–38 (2007).
22. Sun, J. *et al.* High-pressure polymeric phases of carbon dioxide. *Proc. Natl. Acad. Sci.* **106**, 6077–6081 (2009).
23. Datchi, F., Giordano, V. M., Munsch, P. & Saitta, A. M. Structure of carbon dioxide phase IV: Breakdown of the intermediate bonding state scenario. *Phys. Rev. Lett.* **103**, 185701 (2009).
24. Giordano, V. M., Datchi, F., Gorelli, F. A. & Bini, R. Equation of state and anharmonicity of carbon dioxide phase I up to 12 GPa and 800 K. *The J. Chem. Phys.* **133** (2010).
25. Santoro, M. *et al.* Partially collapsed cristobalite structure in the non molecular phase V in CO₂. *Proc. Natl. Acad. Sci.* **109**, 5176–5179 (2012).
26. Datchi, F. *et al.* Structure and compressibility of the high-pressure molecular phase II of carbon dioxide. *Phys. Rev. B* **89**, 144101 (2014).
27. Datchi, F., Moog, M., Pietrucci, F. & Saitta, A. M. Polymeric phase V of carbon dioxide has not been recovered at ambient pressure and has a unique structure. *Proc. Natl. Acad. Sci.* **114**, E656–E657 (2017).
28. Dziubek, K. F. *et al.* Crystalline polymeric carbon dioxide stable at megabar pressures. *Nat. Commun.* **9**, 3148 (2018).
29. Gao, G. *et al.* Dissociation of methane under high pressure. *The J. Chem. Phys.* **133** (2010).
30. Ninet, S. & Datchi, F. High pressure–high temperature phase diagram of ammonia. *The J. Chem. Phys.* **128** (2008).
31. Ojwang, J., Stewart McWilliams, R., Ke, X. & Goncharov, A. F. Melting and dissociation of ammonia at high pressure and high temperature. *The J. Chem. Phys.* **137** (2012).
32. Lipp, M. J., Evans, W. J., Baer, B. J. & Yoo, C.-S. High-energy-density extended CO solid. *Nat. Mater.* **4**, 211–215 (2005).
33. Bonev, S., Lipp, M., Crowhurst, J. & McCarrick, J. Energetics of polymeric carbon monoxide. *The J. Chem. Phys.* **155** (2021).
34. Scelta, D. *et al.* High temperature decomposition of polymeric carbon monoxide at pressures up to 120 GPa. *The J. Chem. Phys.* **159** (2023).
35. Iota, V., Yoo, C. S. & Cynn, H. Quartzlike carbon dioxide: An optically nonlinear extended solid at high pressures and temperatures. *Science* **283**, 1510–1513 (1999).
36. Datchi, F., Mallick, B., Salamat, A. & Ninet, S. Structure of polymeric carbon dioxide CO₂-V. *Phys. Rev. Lett.* **108**, 125701 (2012).
37. Iota, V. & Yoo, C.-S. Phase diagram of carbon dioxide: Evidence for a new associated phase. *Phys. Rev. Lett.* **86**, 5922 (2001).
38. Yoo, C.-S., Sengupta, A. & Kim, M. Phase diagram of carbon dioxide: update and challenges. *High Press. Res.* **31**, 68–74 (2011).
39. Cogollo-Olivo, B. H., Biswas, S., Scandolo, S. & Montoya, J. A. Ab initio determination of the phase diagram of CO₂ at high pressures and temperatures. *Phys. Rev. Lett.* **124**, 095701 (2020).
40. Holm, B., Ahuja, R., Belonoshko, A. & Johansson, B. Theoretical investigation of high pressure phases of carbon dioxide. *Phys. Rev. Lett.* **85**, 1258 (2000).
41. Kim, M., Ryu, Y. J., Lim, J. & Yoo, C.-S. Transformation of molecular CO₂-III in low-density carbon to extended CO₂-V in porous diamond at high pressures and temperatures. *J. Physics: Condens. Matter* **30**, 314002 (2018).
42. Serra, S., Cavazzoni, C., Chiarotti, G., Scandolo, S. & Tosatti, E. Pressure-induced solid carbonates from molecular CO₂ by computer simulation. *Science* **284**, 788–790 (1999).
43. Tschauner, O., Mao, H.-k. & Hemley, R. J. New transformations of CO₂ at high pressures and temperatures. *Phys. Rev. Lett.* **87**, 075701 (2001).

44. Montoya, J. A., Rousseau, R., Santoro, M., Gorelli, F. & Scandolo, S. Mixed threefold and fourfold carbon coordination in compressed CO₂. *Phys. Rev. Lett.* **100**, 163002 (2008).
45. Yong, X. *et al.* Crystal structures and dynamical properties of dense CO₂. *Proc. Natl. Acad. Sci.* **113**, 11110–11115 (2016).
46. Grimme, S., Antony, J., Ehrlich, S. & Krieg, H. A consistent and accurate ab initio parametrization of density functional dispersion correction (DFT-D) for the 94 elements H-Pu. *The J. Chem. Phys.* **132** (2010).
47. Dronskowski, R. & Blöchl, P. E. Crystal orbital Hamilton populations (COHP): energy-resolved visualization of chemical bonding in solids based on density-functional calculations. *The J. Phys. Chem.* **97**, 8617–8624 (1993).
48. Deringer, V. L., Tchougréeff, A. L. & Dronskowski, R. Crystal orbital Hamilton population (COHP) analysis as projected from plane-wave basis sets. *The J. Phys. Chem. A* **115**, 5461–5466 (2011).
49. Maintz, S., Deringer, V. L., Tchougréeff, A. L. & Dronskowski, R. Lobster: A tool to extract chemical bonding from plane-wave based dft (2016).
50. Müller, P. C., Ertural, C., Hempelmann, J. & Dronskowski, R. Crystal orbital bond index: Covalent bond orders in solids. *The J. Phys. Chem. C* **125**, 7959–7970 (2021).
51. Perdew, J. P., Burke, K. & Ernzerhof, M. Generalized gradient approximation made simple. *Phys. Rev. Lett.* **77**, 3865 (1996).
52. Grimme, S., Ehrlich, S. & Goerigk, L. Effect of the damping function in dispersion corrected density functional theory. *J. Comput. Chem.* **32**, 1456–1465 (2011).
53. Peng, H., Yang, Z.-H., Sun, J. & Perdew, J. P. SCAN+rVV10: A promising van der Waals density functional. *arXiv preprint arXiv:1510.05712* (2015).
54. Román-Pérez, G. & Soler, J. M. Efficient implementation of a van der Waals density functional: application to double-wall carbon nanotubes. *Phys. Rev. Lett.* **103**, 096102 (2009).
55. Mejia-Rodriguez, D. & Trickey, S. Deorbitalization strategies for meta-generalized-gradient-approximation exchange-correlation functionals. *Phys. Rev. A* **96**, 052512 (2017).
56. Sun, J., Xiao, B. & Ruzsinszky, A. Communication: Effect of the orbital-overlap dependence in the meta generalized gradient approximation. *The J. Chem. Phys.* **137** (2012).
57. Becke, A. D. Density-functional thermochemistry. I. The effect of the exchange-only gradient correction. *The J. Chem. Phys.* **96**, 2155–2160 (1992).
58. Heilweil, E., Moore, R., Rothenberger, G., Velsko, S. & Hochstrasser, R. Picosecond processes in chemical systems: Vibrational relaxation. *Laser Chem.* **3**, 109–132 (1983).
59. Citroni, M. Real-time bond formation. *Nat. Rev. Chem.* **4**, 64–64 (2020).
60. Liu, Y. *et al.* Rehybridization dynamics into the pericyclic minimum of an electrocyclic reaction imaged in real-time. *Nat. Commun.* **14**, 2795 (2023).
61. Lundegaard, L. F., Weck, G., McMahon, M. I., Desgreniers, S. & Loubeyre, P. Observation of an O₈ molecular lattice in the ϵ phase of solid oxygen. *Nature* **443**, 201–204 (2006).
62. Anh, L. T., Wada, M., Fukui, H., Kawatsu, T. & Iitaka, T. First-principles calculations of the epsilon phase of solid oxygen. *Sci. Reports* **9**, 8731 (2019).
63. Born, M. & Heisenberg, W. Zur quantentheorie der molekeln. *Orig. Sci. Pap. Wissenschaftliche Orig.* 216–246 (1985).
64. Kresse, G. & Hafner, J. Ab initio molecular dynamics for liquid metals. *Phys. Rev. B* **47**, 558 (1993).
65. Kresse, G. & Furthmüller, J. Efficiency of ab-initio total energy calculations for metals and semiconductors using a plane-wave basis set. *Comput. Mater. Sci.* **6**, 15–50 (1996).
66. Kresse, G. & Furthmüller, J. Efficient iterative schemes for ab initio total-energy calculations using a plane-wave basis set. *Phys. Rev. B* **54**, 11169 (1996).
67. Perdew, J. P. *et al.* Atoms, molecules, solids, and surfaces: Applications of the generalized gradient approximation for exchange and correlation. *Phys. Rev. B* **46**, 6671 (1992).
68. Baldereschi, A. Mean-value point in the Brillouin zone. *Phys. Rev. B* **7**, 5212 (1973).
69. Freiman, Y. A. Magnetic properties of solid oxygen under pressure. *Low Temp. Phys.* **41**, 847–857 (2015).

70. Kaplan, A. D., Shahi, C., Bhetwal, P., Sah, R. K. & Perdew, J. P. Understanding density-driven errors for reaction barrier heights. *J. Chem. Theory Comput.* **19**, 532–543 (2023).
71. Kanungo, B., Kaplan, A. D., Shahi, C., Gavini, V. & Perdew, J. P. Unconventional error cancellation explains the success of Hartree–Fock density functional theory for barrier heights. *The J. Phys. Chem. Lett.* **15**, 323–328 (2024).
72. Tan, C. W. *et al.* High-performance training and inference for deep equivariant interatomic potentials. *arXiv preprint arXiv:2504.16068* (2025).
73. Musaelian, A. *et al.* Learning local equivariant representations for large-scale atomistic dynamics. *Nat. Commun.* **14**, 579 (2023).
74. Kozinsky, B., Musaelian, A., Johansson, A. & Batzner, S. Scaling the leading accuracy of deep equivariant models to biomolecular simulations of realistic size. In *Proceedings of the International Conference for High Performance Computing, Networking, Storage and Analysis*, 1–12 (2023).
75. Thompson, A. P. *et al.* LAMMPS—a flexible simulation tool for particle-based materials modeling at the atomic, meso, and continuum scales. *Comput. physics communications* **271**, 108171 (2022).
76. Baroni, S., De Gironcoli, S., Dal Corso, A. & Giannozzi, P. Phonons and related crystal properties from density-functional perturbation theory. *Rev. Mod. Phys.* **73**, 515 (2001).
77. Togo, A. First-principles phonon calculations with Phonopy and Phono3py. *J. Phys. Soc. Jpn.* **92**, 012001 (2023).

Acknowledgements

We thank C.S. Yoo for discussions. This work was performed under the auspices of the U.S. Department of Energy by Lawrence Livermore National Laboratory (LLNL) under contract number DEAC52-07NA27344. The authors acknowledge funding support from the DOE Laboratory Directed Research and Development (LDRD) program at LLNL under the project tracking code 23-ER-028.

Author contributions

J.C.C. and S.A.B. designed research; R.P. performed research; S.A.B. supervised research; R.P. and S.A.B. wrote the paper; J.C.C. provided guidance; all authors discussed the results and contributed to the final manuscript.

Additional information

Correspondence and requests for materials should be addressed to S.A.B.